ELECTRON-CLOUD EFFECTS IN
HIGH-INTENSITY PROTON ACCELERATORS*

Jie Wei[†], Brookhaven National Laboratory, Upton, New York 11973, USA
Robert J. Macek, Los Alamos National Laboratory, New Mexico 87545, USA

Abstract

One of the primary concerns in the design and operation of high-intensity proton synchrotrons and accumulators is the electron cloud and associated beam loss and instabilities. Electron-cloud effects are observed at high-intensity proton machines like the Los Alamos National Laboratory's PSR and CERN's SPS, and investigated experimentally and theoretically. In the design of next-generation high-intensity proton accelerators like the Spallation Neutron Source ring, emphasis is made in minimizing electron production and in enhancing Landau damping. This paper reviews the present understanding of the electron-cloud effects and presents mitigation measures.

1 INTRODUCTION

Electron-cloud effects are important, but incompletely understood dynamical phenomena. Effects that can severely limit the performance of high-intensity proton synchrotrons include trailing-edge tune-shift and resonance crossing, electron-proton instability, emittance growth and beam loss, increases in vacuum pressure, heating of the vacuum pipe, and interference with beam diagnostics. The following are examples of hadron rings where electron-cloud effects are observed: Proton Storage Ring (PSR) at the Los Alamos National Laboratory (LANL), where a strong, fast transverse-instability occurs both for coasting and bunched beam when a threshold intensity is exceeded [1]; CERN's PS and SPS, where a large number of electrons are produced by beam-induced multipacting when the machine's parameters are configured for LHC injection [2, 3]; and, BNL's Relativistic Heavy Ion Collider (RHIC) where the vacuum pressure dramatically increases when the beams are injection with halved nominal bunch-spacing. The electron-cloud effects can limit the performance of the next-generation high-intensity proton rings, such as the Spallation Neutron Source (SNS) accumulator ring [4], the Large Hadron Collider (LHC) [5], and neutrino factory's proton-drivers.

This paper attempts to summarize the present understanding of the electron-cloud effects pertaining to high-intensity proton synchrotrons and accumulators. Section 2 describes some typical phenomena. Section 3 identifies the main sources of electron generation including stripping injection, proton grazing at the collimator surfaces, beam-induced multipacting, and gas ionization. The effects of

electron cloud on the proton beam are discussed in Sections 4 and 5. Preventive methods are described in Section 6. Finally, a summary is given in Section 7.

2 PHENOMENA

In the recently commissioned Relativistic Heavy Ion Collider (RHIC) [6], vacuum-pressure rises were observed during high-intensity operation of both gold- and proton-beams. As shown in Figure 1, beam injection with halved bunch spacing resulted in a much higher vacuum pressure than the normal value [7, 8]. The pressure rise occurred when the total beam intensity in the ring is only 60% of the nominal intensity. The dominant mechanism is suspected to be the electron cloud [7].

A fast, vertical instability was observed at Brookhaven's AGS Booster when the proton beam was debunched. After the beam was injected, the beam suffered a 10% slow-loss over about 1 ms and then a 60% fast-loss over tens of micro-seconds. Accompanying the fast beam-loss was instability in the vertical direction. The threshold could vary by a factor of 2 from a peak current of 2.7 A to 5.3
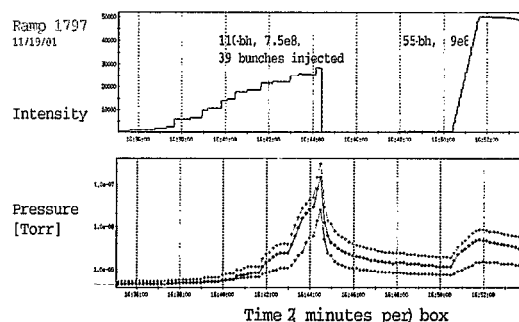

Figure 1: Vacuum-pressure rise in RHIC during gold-beam injection (courtesy S. Y. Zhang and the RHIC crew). The top curve indicates the total beam intensity as a function of time, and the bottom curves indicate the corresponding vacuum pressure at one location (BO11) of the ring. The horizontal scale is 2 minutes per box. The right-hand side shows the nominal operation when 55 bunches, each containing 9×10^8 gold ions, are injected into the ring. The left-hand side shows that when the bunch spacing is reduced in half, the vacuum pressure increases dramatically even when only 39 bunches, each containing 7.5×10^8 gold ions, are injected.
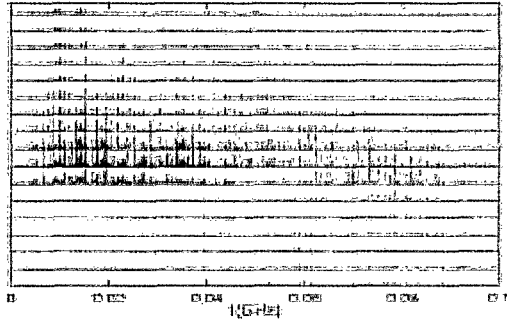
Figure 2: Beam-Position-Monitor (BPM) difference signal of a debunched proton-beam measured in the AGS Booster indicating an instability in the vertical direction (courtesy M. Blaskiewicz). The vertical axis is the spectral amplitude of the BPM's sum (blue) and difference (red) signals. Every trace is 12 μs apart. The horizontal and vertical tunes are 4.8 and 4.95, respectively.
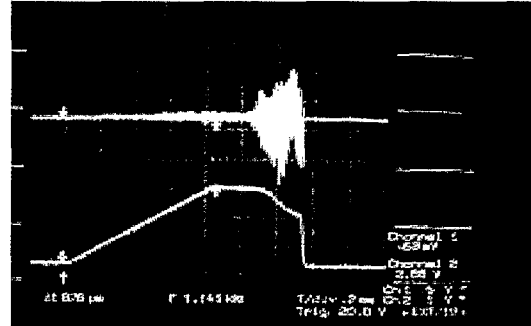

Figure 3: Fast instability observed at PSR. The top curve is the vertical difference signal of the BPM, and the bottom curve is from the beam-loss monitor. The horizontal scale is 0.2 ms per box. The total beam charge is 4.2 μC. The RF voltage is 13.5 kV.

A depending on the vertical betatron tune. As shown in Figure 2, the characteristic frequency of instability was between 80 and 100 MHz. Possible mechanisms included the trapping of electrons when the proton beam-gap was eliminated [9].

In LANL's PSR, a strong, fast transverse-instability occurred both for coasting and bunched beams when a threshold intensity was exceeded [10]. The phenomenon limited the ring's achievable intensity. Depending on the lattice optics (e.g., sextupole and skew-quadrupole settings), the instability could be in either horizontal or vertical direction. As shown in Figure 3, the instability's growth time was about 75 μs (or 200 turns). The frequency spectrum was from 70 to 200 MHz corresponding to the bouncing frequency of the electrons. The threshold intensity was linearly proportional to the RF voltage applied on the beam (Figure 4). A large amount of electrons was measured on the beam vacuum-pipe with a time structure closely correlated to the passage of the proton beam.

3 ELECTRON GENERATION

We classify electron production into the following categories: (1) electrons generated at the stripping foil in the injection region; (2) electrons generated at the surfaces of collimators and vacuum pipe due to the impact of lost protons; (3) electrons produced by beam-induced multipacting from the vacuum-pipe's wall; and, (4) electrons produced around the ring from residual-gas ionization.

Figure 5 shows the distribution of electron-density flux measured at the PSR using the electron detector developed at the Argonne National Laboratory [11]. The quantity f_e is defined as the ratio of the number of electrons striking the vacuum pipe within one turn to the number of stored protons in the ring, scaled from the area of the detector surface. The electron density is high at the injection region
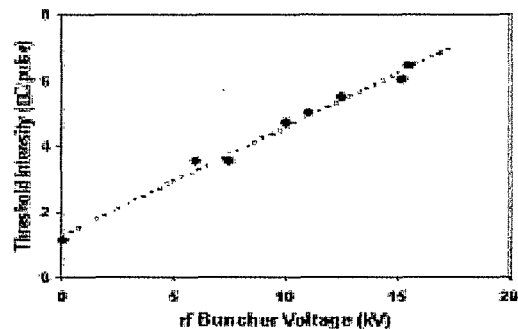

Figure 4: Intensity threshold of the transverse instability as a function of the RF voltage at the PSR.

where the H^- beam is stripped of its electrons, and high at the extraction region due to limited apertures.

3.1 Injection Region

Multi-turn charge-exchange injection is often preferred for high-intensity rings to enhance the phase-space density of the accumulated beam. The charge-exchange process is performed with a stripping foil typically of density from 200 to 400 $\mu g/cm^2$ (about 1μm thick). Near the injection stripping-foil, a high concentration of electrons is expected with a broad energy-spectrum. With a H^- beam, the stripped electrons carry twice the current of the injecting H^- beam with a kinetic energy of $m_e c^2(\gamma - 1)$, where γ is the relativistic factor of the H^- beam. The injecting- and circulating-beams impacting on the foil produce secondary emission of electrons at low energy (tens of eV). Although the yield is low (0.006 for a 800-MeV proton beam incident on carbon material), the effect is proportional to the number of traversals of the foil. The injecting- and circulating-beam also produce knock-on electrons at a high energy (up to several MeV). The stripping foil, operating at
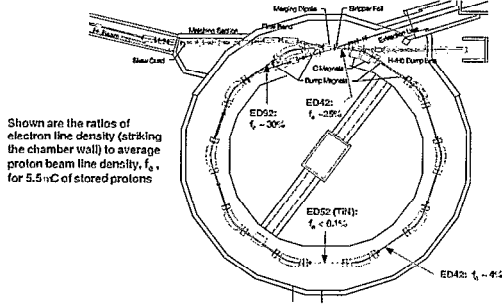
Figure 5: Distribution of the electron flux measured on the wall of the vacuum pipe at the PSR. The circumference of the ring is 90.2 m. The kinetic energy of the proton beam is 800 MeV. The flux ratio f_e, varying around the ring, is about 30% downstream of the extraction septum, about 25% downstream of the injection stripping-foil, about 4% in section 4, and within the noise level in the TiN-coated section 5.

a high temperature around 2000 K, emits thermionic electrons at low energy. All these electrons may back-scatter from the stripped-electron collector and the surrounding surfaces [12]. As an example, Table 1 lists the sources of production, yield, and energy-range of the electrons at the PSR's injection region [13].

Figure 6 illustrates the collection of stripped-electrons at the SNS accumulator ring. The electrons are guided by a magnetic field and collected by a water-cooled device of heat-resistant material. The electron collector uses a carbon material attached to water-cooled copper plate [14]. Selecting a low-charge-state material for the collector also reduces the number of back-scattered electrons. Figure 7 shows the temperature distribution at the electron collector when the stripped-electron beam of 3 kW power strikes the surface of about 1 cm^2 area.

Table 1: Estimated yield and kinetic energy of the electrons produced by the injected H$^-$ beam at the PSR. The yield is defined as the ratio of total number of electrons produced during the accumulation period per injected H$^-$ particle. The average number of foil traversal is about 50. The kinetic energy of the injecting beam is 800 MeV. The average H$^-$ beam current is 100μA (courtesy M. Plum).

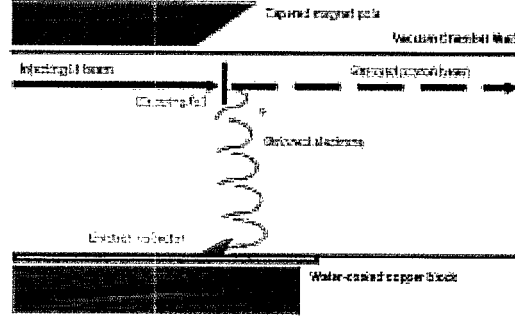| Source	Yield	Kinetic energy
Stripped e^-	2.0	430 keV
Secondary e^-	1.0	up to 20 eV
Knock-on e^-	0.4	up to 2.4 MeV
Thermionic e^-	< 0.002	~0.24 eV
Ionization	0.02	up to 2.4 MeV

Figure 6: Collection of stripped electrons during the injection of H$^-$ beam at the SNS accumulator ring.
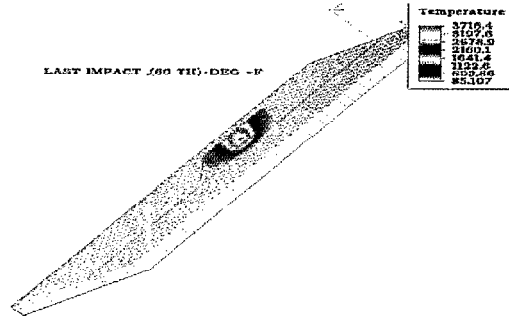

Figure 7: Temperature (F) distribution at the stripped-electron collector at the SNS ring in units of Fahrenheit (or $5F/9 + 255.37$ K, Courtesy C. J. Liaw and J. Brodowski).

3.2 Collimation Region

The region near the scrapers and collimators is susceptible to a high beam-loss and, potentially, is another location of high electron-concentration. Protons incident on the collimators' surfaces produce secondary electrons. Depending on the energy of the beam and the incident angle, the secondary electron-to-proton yield can greatly exceed 1 when the incident beam is nearly parallel to the surface (i.e., grazing angle $\theta_g \approx \pi/2$). Experiments were performed with different ions at Brookhaven's Tandem accelerator to verify the angular dependence of electron yield [15]. As shown in Figure 8, the proton-induced yield Y_{ep} has a $1/\cos\theta_g$ dependence on the grazing angle θ_g, similar to the electron-induced secondary-emission yield as predicted by the Seiler model based on experimental fits [16, 17, 18, 7]

$$Y_{ep} = \frac{1.11 Y_{ep}^{max} \left\{ 1 - \exp\left[-2.3 \left(\frac{E_k}{E_k^{max}} \right)^{1.35} \right] \right\}}{\left(\frac{E_k}{E_k^{max}} \right)^{0.35} \cos\theta_g} \quad (1)$$

where E_k is the kinetic energy of the primary proton, and the proton energy that corresponds to the maximum yield,

E_k^{max}, is about 0.7 MeV. A serrated surface with triangular teeth greatly reduced the generation of secondary-emission electrons. However, at the beam energy around 1 GeV the proton stopping-length is long (about one meter). A serrated surface may be ineffective since protons incident on the front edge of the teeth may easily escape from the collimator body. The SNS ring uses a two-stage collimation system so that the beam's halo is likely to be incident on the front edge of the secondary collimators consisting of layers of stainless-steel blocks, stainless-steel balls, borated water, and lead shield. Figure 9) shows one of three secondary collimators [19]. The primary scraper consists of four adjustable, thin tantalum-blades spaced in 45 degree angles, and shielded for radioactivation containment.
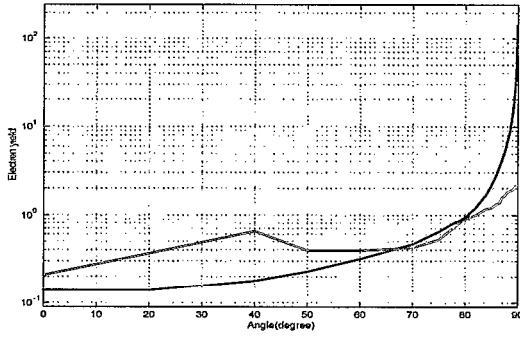

Figure 8: Proton-induced secondary-emission yields of electrons as functions of the incident angle for 28-MeV protons striking a flat (blue) and a serrated (red) stainless-steel surface (courtesy P. Thieberger).
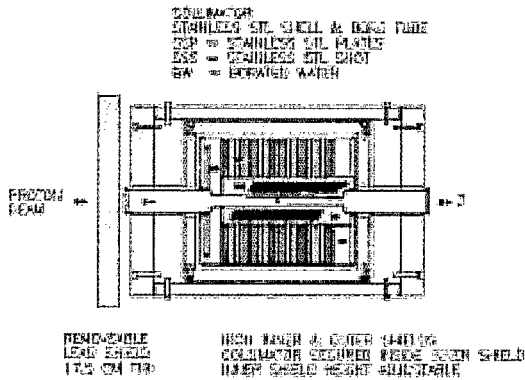

Figure 9: Schematics of one of SNS ring's secondary collimators showing layers of material for radio-activation containment (courtesy H. Ludewig and N. Simos). The effective length is about 1.5 m. The collimator is designed to withstand an average beam power of up to 10 kW at 1 GeV kinetic energy.
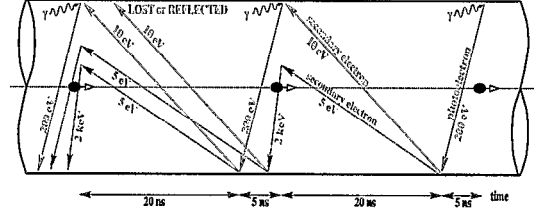

Figure 10: Electron build-up at CERN's LHC as an example of multibunch, beam-induced electron multipacting (courtesy F. Ruggiero). The time between successive bunches is 25 ns. The energy gain due to the bunch passage is about 200 eV.

3.3 Beam-induced Multipacting

Beam-induced multipacting is believed to be the leading source of sustained electron-production. Depending on the beam's parameters, one of the two multipacting models applies: multibunch passage multipacting [20, 21, 22, 23, 24], or single-bunch, trailing-edge multipacting [1, 25].

The phenomena of multibunch, beam-induced multipacting were observed at the CERN's PS and SPS when the machines' parameters were configured for LHC injection parameters. The electron-cloud buildup was sensitive to the intensity, spacing, and length of the proton bunches, and to the secondary-emission yield (SEY) of electrons from the beam-pipes' surfaces.

As shown in Figure 10, the multibunch multipacting occurs if the transit time of the electrons crossing the vacuum pipe is comparable to the time between successive bunches, and if the electrons gain enough energy to produce more than one secondary-electrons when it hits the vacuum-pipe's wall [20]. The multipacting parameter ζ_m is defined as the ratio between the transit time of the electrons crossing the vacuum pipe to the time between successive bunches

$$\zeta_m = \frac{2b}{s_b} \frac{\beta}{\beta_e} \qquad (2)$$

where b is the radius of the vacuum pipe, s_b is the distance between the subsequent bunches, β is the velocity of the proton normalized by the speed of light c, and $\beta_e c$ is the average velocity of the electrons. Here, β_e is related to the energy gained by the electron from the passage of the proton bunch

$$\Delta E_e = m_e c^2 \left[\sqrt{\left(\frac{2r_e N_0}{\beta b}\right)^2 + 1} - 1 \right] \qquad (3)$$

where $r_e = e^2/4\pi\epsilon_0 m_e c^2$ is the classical radius of electron, and N_0 is the number of protons in the bunch. When the electrons' motion is non-relativistic, i.e.,

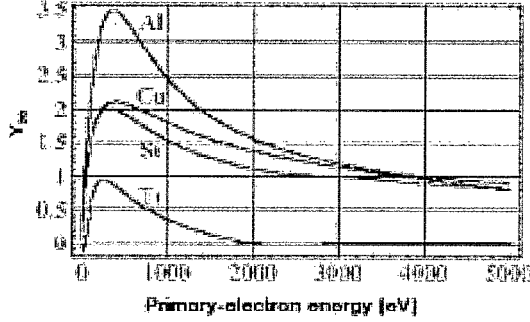$$\frac{2r_e N_0}{\beta b} \ll 1 \qquad (4)$$

Figure 11: Secondary-electron yield Y_{ee} as a function of the primary-electron energy for a perpendicular incidence and for technical surfaces representative of vacuum pipes (courtesy N. Hilleret and O. Gröbner).
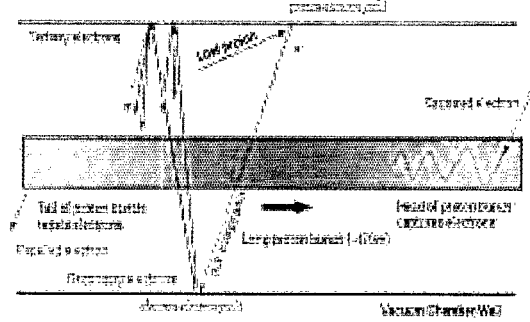

Figure 12: Beam-induced electron multipacting at the trailing edge of a long proton-bunch. The transit time of the electrons across the beam pipe is much shorter than the passage time of the proton bunch.

Eqs. 2 and 3 can be approximated as [20]

$$\zeta_m \approx \frac{\beta^2 b^2}{r_e N_0 s_b} \tag{5}$$

and

$$\Delta E_e \approx 2 m_e c^2 \left(\frac{r_e N_0}{\beta b} \right)^2 \tag{6}$$

The condition for proper multibunch multipacting is given by

$$\zeta_m = 1 \tag{7}$$

The energy gained by the electron must be such that the electron-induced secondary-emission yield (SEY) satisfies

$$\alpha_e Y_{ee} > 1 \tag{8}$$

where $\alpha_e \leq 1$ is electron's survival rate in the bunch gap [7]. Figure 11 shows the typical electron-induced SEY (Y_{ee}) as a function of the primary-electron energy for a perpendicular incidence.

Multibunch electron multipacting may occur for almost any value of ζ_m [26]. The exact resonance condition is met if $\zeta_m = 1$. If $\zeta_m > 1$, the primary electrons interact with more than one proton bunch; If $\zeta_m \leq 1$, part of the primary electrons is lost before the next bunch arrives, leaving behind less-energetic secondary particles (PS, SPS). On the other hand, if $\zeta_m \ll 1$, the electron cloud is usually dominated by single-bunch multipacting. In fact, since here the transit time of the electrons across the vacuum chamber is typically much shorter than the passage time of the proton bunch, the energy gained by the electrons is much lower than that predicted by the multibunch multipacting model (Eqs. 3 and 6).

Single-bunch, trailing-edge multipacting starts to dominate if the bunch length is long enough to sustain multiple passes of electrons. As shown in Figure 12, electrons are attracted towards the rising edge of the proton bunch. At the trailing edge of the proton bunch, electrons are released and yet still accelerated by the bunch to multipact.

The number of electrons grows exponentially at the trailing edge of the proton bunch, as observed at the PSR (Figure 13) [10]. The electron-cloud buildup due to this single-bunch mechanism is expected to have a weak dependence on the bunch spacing, the vacuum-pressure level, and the amount of residual protons in the beam gap. On the other hand, it depends critically on the length of the proton bunch and the variations in its longitudinal density.

Similar to the multibunch parameter ζ_m (Eq. 5), single-bunch multipacting parameter ζ_s can be defined as the ratio between the transit time of the electrons crossing the vacuum pipe to the passage time of the proton-bunch's trailing-edge

$$\zeta_s = \frac{b}{s_b B_f} \frac{\beta}{\beta_e} \tag{9}$$

where the effective length of the proton bunch is $s_b B_f$, the bunching factor, $B_f \leq 1$, is defined as the ratio between the average and peak line-density of the proton beam, and

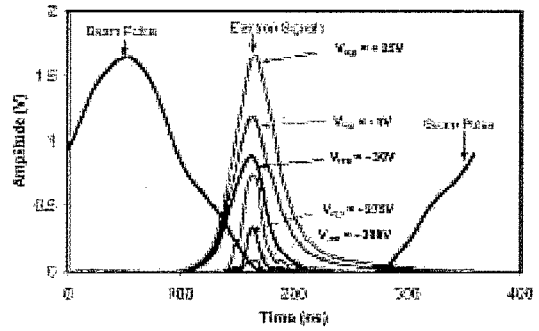$$\zeta_s > \zeta_m \tag{10}$$

Figure 13: Electron signals measured at the PSR as a function of time relative to the proton-beam pulse during a single revolution. The repeller voltage, V_{rep}, is varied to select the electrons striking the detector according to their energy.
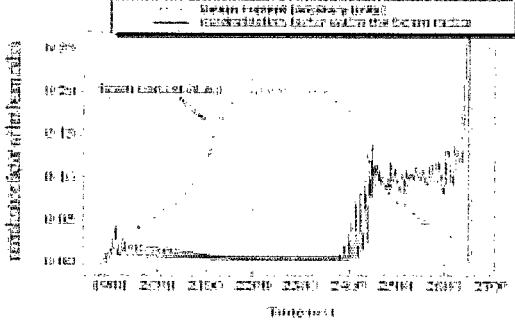
Figure 14: Computer simulation of electron generation in the SNS accumulator ring (courtesy M. Pivi and M. Furman). The neutralization factor is defined as the density ratio between the electron and proton within the proton beam-radius. The beam intensity is 2×10^{14} per bunch. The peak secondary-emission yield is assumed to be 2. The full bunch-length is about 700 ns.

To obtain an order-of-magnitude estimate, assume that the beam charge is uniformly distributed in the transverse directions in the vacuum chamber. The average velocity of the electron is given in the non-relativistic limit

$$\beta_e \approx \sqrt{\frac{r_e N_0}{s_b B_f}} \ll 1 \qquad (11)$$

Eq. 9 thus becomes

$$\zeta_s \approx \frac{\beta b}{\sqrt{r_e N_0 s_b B_f}} \qquad (12)$$

The energy gained by the electron is approximately

$$\Delta E_e \approx 4 m_e c^2 \beta b \sqrt{\frac{r_e N_0}{s_b^3 B_f^3}} \qquad (13)$$

Single-bunch multipacting occurs if the condition

$$\zeta_s \ll 1 \qquad (14)$$

is satisfied, and if the energy gained by the electron is such that

$$Y_{ee} > 1 \qquad (15)$$

As an example, consider the SNS ring parameters: $N_0 = 2 \times 10^{14}$, $s_b = 248$ m, $B_f \approx 0.5$, $b \approx 0.1$ m, and $\beta = 0.875$. The single-bunch multipacting parameter is $\zeta_s \approx 0.01 \ll 1$. The characteristic energy gain is approximately $\Delta E_e \approx 97$ eV. Single-bunch, trailing-edge multipacting is expected to occur, as shown by the computer simulation in Figure 14 [27].

The actual multipacting process may be a combination of the single- and multibunch multipacting. Figure 15 shows the measured secondary-emission spectrum used for simulation consisting of true-secondary, back-scattered, and re-diffused electrons [28]. Uncertainties remain in key parameters describing the interactions of low-energy (< 20 eV) electrons with the accelerator surfaces.
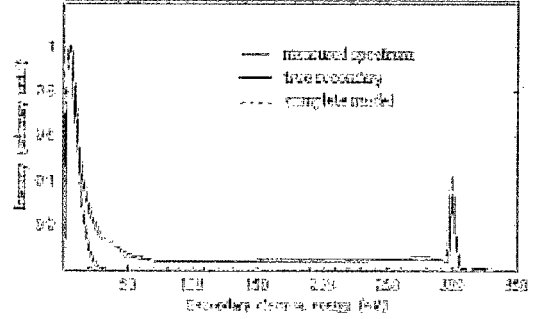

Figure 15: Secondary-emission energy-spectrum used for simulations (Hilleret fit Cu) for a 300 eV incident-electron beam. The rediffused and reflected components are included in the model (courtesy M. Pivi and M. Furman).

3.4 Ionization

The rate of electron production by gas ionization is linearly proportional to the proton's beam-current I, the vacuum pressure P, and the ionization cross-section σ_{ion} [26, 7]. The rate of electron line-density increase per unit length of circumference is given by the relation

$$\frac{d^2 \lambda_e}{dt ds} = \frac{\rho_m \beta I \sigma_{ion} P}{e} \qquad (16)$$

where P is in units of Torr (1 Torr $= 133.3$ Pascal). At the room temperature of 300 K, the molecular density ρ_m is about 3.3×10^{22} m^{-3}. For the SNS ring at a pressure of 10^{-8} Torr, a total of 2.6×10^9 electrons is produced per turn when the proton accumulation reaches 2×10^{14}. This is much fewer than the electrons produced at the bunch's trailing edge when multipacting occurs. The effect of photoemission usually is negligible for medium-energy protons due to lack of synchrotron radiation.

Various computer-simulation programs were developed to model the process of electron generation [30, 31, 21]. Simulated mechanisms included space-charge fields of both the protons (or e^+) and electrons, vacuum pipe and the image charges, external magnetic-fields, gas ionization, secondary emission, and photoemission. Recent developments incorporated trailing-edge multipacting, re-diffusion, back-scattering, and proton-induced secondary emission with refined angular dependence of the incident particle [27, 32, 29]. Particle-in-cell (PIC) algorithms were also developed to model detailed electron-generation processes [33].

4 ELECTRON NEUTRALIZATION AND TUNE SHIFT

4.1 Electron Bounce-frequency

The electron motion is characterized by the electron bouncing-frequency

$$\omega_e \approx c\sqrt{2\pi r_e n_p} \qquad (17)$$

where n_p is the volume density of the proton beam. Figure 16 shows the frequency spectra of the BPM's vertical difference-signal measured at the PSR for two beam intensities. The peak spectrum for the 6.1 mC beam-intensity centers around 200 MHz, corresponding to the electron bounce-frequency. When the intensity is reduced by a factor of two by injecting every other pulse, the mean frequency of the peak spectrum shifts downwards by a factor of about 0.7.
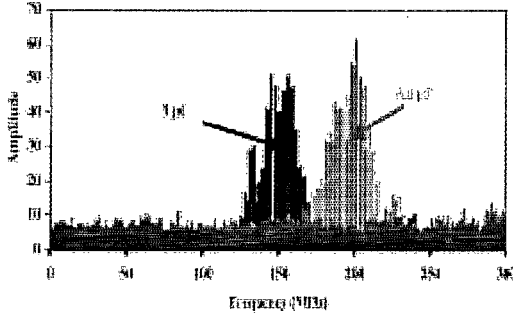

Figure 16: Frequency-spectrum of BPM's vertical difference-signal for two beam intensities measured at the PSR. The lines in the peaks are the betatron side-bands.

4.2 Neutralization Tune-shift

In high-intensity synchrotrons, protons' tune shifts can be attributed to various mechanisms: space charge, chromaticity, kinematic nonlinearity, magnetic nonlinearity, and magnetic fringe field. The dominant contribution is usually from the space charge at the injection energy. Beam loss is often caused by resonance crossing associated with an excessive amount of tune spread in the beam. Figure 17 shows the spread of tune shift of a 2 MW proton-beam in the absence of electron cloud at the SNS accumulator ring.

An electron cloud tends to neutralize the positive charge of the proton beam. Compared to the space-charge tune-shift between the protons, the tune shift produced by the electron cloud is enhanced by a factor γ^2 due to absence of the compensating electric and magnetic forces in the laboratory frame. With the electron cloud, the space-charge

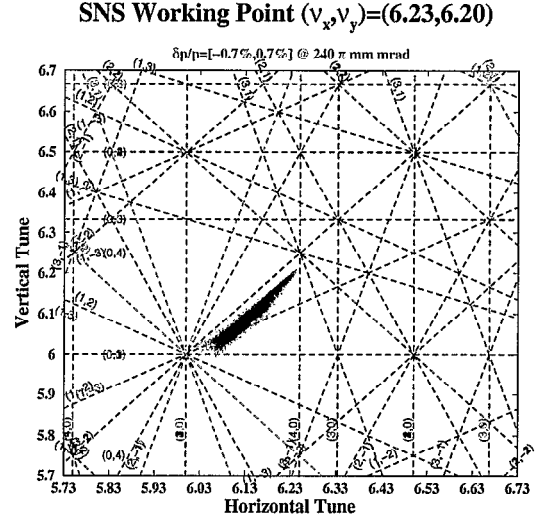### SNS Working Point $(\nu_x,\nu_y)=(6.23,6.20)$

Figure 17: Spread of tune shift of a 2 MW proton beam in the SNS accumulator ring. The computer-simulation results are obtained with the Unified-Accelerator-Libraries (UAL) package [34]. Structure resonances are indicated in red.

tune-shift becomes

$$\Delta\nu_{x,y} = -\frac{f_{sc}N_0 r_0 R_0}{2\pi B_f \nu_{x,y,0}\beta^2\gamma}\left[\frac{1}{\sigma_{x,y}(\sigma_x+\sigma_y)}\left(\frac{1}{\gamma^2}-\eta_e\right)\right.$$
$$\left. + A_{im}\left[\gamma^{-2}-\eta_e\right]\right] \qquad (18)$$

where $r_0 = e^2/4\pi\epsilon_0 m_0 c^2$ is the classical radius of proton, R_0 is the average radius of circumference, $\nu_{x,0}$ and $\nu_{y,0}$ are the base transverse tunes, and σ_x and σ_y are the horizontal- and vertical-rms beam sizes. The bunch's form-factor f_{sc} is equal to $1/2$ for an uniform distribution, and to 1 for a Gaussian distribution. The neutralization factor (η_e), defined as the electron-to-proton density ratio in the laboratory frame, represents the contribution of electron cloud at a low energy (typically up to several hundreds eV). The contribution from the image charge of the beam is represented by the Laslett tune-shift function $A_{im}\left[\gamma^{-2}-\eta_e\right]$, which includes the effect of the electron neutralization [35]. For both incoherent and coherent space-charge tune-shifts, the relative contribution of the electron cloud is $-\gamma^2\eta_e$.

4.3 Trailing-edge "Pacman" Effect

With the trailing-edge electron-multipacting model, protons at the trailing edge of the bunch experience, on average, a high concentration of electrons. Electron neutralization increases the transverse tunes and possibly increases the tune spread of the beam. When the beam is stored in the ring for an extended time, the bunch may continuously lose its trailing-edge particles upon resonance crossing, i.e., here so-called trailing-edge Pacman effect.

Figure 14 shows the structure of electron neutralization inside the proton bunch at the SNS accumulator ring, predicted from a computer simulation [27]. With a 2-MW beam in the SNS ring, the peak tune-shift due to space charge is about -0.2. The neutralization level is about 10% ($\eta_e \approx 0.1$) inside the proton beam for trailing-edge particles at 50% of the peak longitudinal-density. The tune shift due to electron cloud is about $+0.04$. Given the same space-charge tune-spread at injection, this effect becomes more important for injections at a higher energy.

5 ELECTRON-PROTON INSTABILITIES

Experimental observations of electron-cloud instabilities are distinctively different for "short bunches" stored at energies above the ring's transition energy where multibunch multipacting is expected to be important (PS, SPS, and B-factories), and "long bunches" stored at energies far below the ring's transition energy where single-bunch, trailing-edge multipacting is expected to be dominant (PSR and SNS).

5.1 Coasting-beam and Long-bunch Regime

During the 1970s, coupled oscillations associated with electron trapping and multipacting hindered high-intensity coasting-beam operation at CERN's ISR [36, 37, 20]. The problem was alleviated by installing clearing electrodes around the ring. Since 1988, a fast, vertical instability accompanied by beam loss, both with bunched and un-bunched beams, was attributed to coupled electron-proton oscillations [38, 10]. At BNL's AGS Booster, an intense proton-beam became vertically unstable when it was de-bunched.

The threshold of electron-proton instability is associated with the amount of Landau damping caused by the beam's momentum spread [39]. Figure 4 shows the measured dependence of the threshold intensity on the RF voltage for a given length of injected bunch. The threshold scaling is different from that of transverse instability due to conventional coupling-impedance, where the threshold intensity is proportional to the RF voltage squared. The linear dependence of the threshold results from the dependence of the instability's frequency on the beam's intensity [32]. In fact, at the electron bounce-frequency, ω_e, the transverse frequency-spread is mostly contributed by the momentum slip, i.e.,

$$\frac{\omega_e}{\omega_0} \gg \nu_{x,y}; \quad |\eta|\omega_e \gg \xi_{x,y}\omega_0 \qquad (19)$$

where ω_0 is the angular revolution frequency, η is the momentum-slip factor, $\nu_{x,y}$ are the transverse tunes, and $\xi_{x,y}$ are the chromaticities. The threshold for the transverse stability is

$$|Z_{\perp x,y}| \leq F_\perp \frac{4|\eta|E_s}{\sqrt{\pi}e^2\omega_0 a\langle\beta_\perp\rangle} \sqrt{\frac{B_f R_0 r_e}{N_0}} \left(\frac{\Delta p}{p}\right)_{FWHM} \qquad (20)$$

where $\left(\frac{\Delta p}{p}\right)_{FWHM}$ is the full-width, half-maximum momentum spread of the beam, E_s is the total energy of the proton, $F_\perp$ is the form factor, and a is the average beam radius. With a given coupling-impedance, the threshold intensity is linearly proportional to the momentum-spread squared, and is insensitive to the machine chromaticity. Also, the scaling behavior is extended from bunched beams to a coasting beam as the RF voltage is lowered.

Several theoretical approaches were used to study instabilities of the coupled electron-proton motion. Centroid models of rigid beams provided estimates of the unstable dipole-modes and their scaling with intensity for coasting-beams. They offered plausible predictions for the threshold intensities of instability, given the uncertainties about parameters such as average neutralization [38, 40]. However, estimates of growth rates and behavior beyond threshold showed poor agreement with observations. The centroid models were extended to bunched beams to better model the trailing-edge electron concentration, the instability threshold, and the structure and growth rates above the threshold [32]. Another approach was to develop fully kinetic simulations based on self-consistent solutions of the Maxwell-Vlasov equations for coasting beams in a smooth-focusing approximation [41].

5.2 Short-bunch Regime

The short-bunch regime included instabilities that occurred at most lepton (e^+) rings (KEK's photon factory PF, B-factory KEKB, and BEPC), as well as proton rings (PS and SPS) when the beams were prepared for collider uses [26]. Coupled-bunch, transverse instabilities were observed at KEK PF [42, 30] and BEPC [43], and at SPS (horizontal direction) with the LHC proton test-beams [44]. The electron cloud coupled the motion of subsequent bunches similar to a multibunch wake field. With computer simulations, the effective wake fields were computed to predict the multibunch growth-rates.

Single-bunch, transverse (strong and regular head-tail, fast blow-up) instabilities were identified first at KEK's B-factory and then at CERN's SPS (vertical direction) and PS with the LHC proton test-beams. The electron cloud coupled the head and tail of the bunch similar to a short-range wake-field. A broadband-resonator model was used to describe the coupling-impedance with the resonator frequency at the electron bounce-frequency [45]. Such single-bunch instabilities were often sensitive to ring's chromaticity.

Theoretically, beam break-up treatment [46, 47] and two-particle model [48] were used to obtain the threshold and growth time of the instability assuming that the electron production saturated near the neutralization density. Transverse mode-coupling (TMCI) calculation using simulated wake-field was further used [49]. The instability threshold was found to be linearly proportional to the average electron-density (i.e., N_0/s_b). Recently, particle-in-cell (PIC) simulations based on strong-strong models were

performed [50, 51].

6 PREVENTIVE MEASURES

Control of the electron-cloud effects involves suppressing electron generation and enhancing Landau damping. The number of multipacting-electrons can be effectively reduced by surface treatment of the vacuum pipe. Electrons in the injection region need to be guided to the collectors with a low back-scattering yield [12]. A beam-in-gap kicker can ensure a clean beam-gap [52, 53, 54]. Vacuum ports can be screened, and steps in the vacuum pipe can be tapered to reduce peaked electric fields causing electron emission. A relatively good vacuum can reduce electrons from gas ionization. Solenoids can be wound in straight sections to reduce multipacting [55, 56]. Electrodes can be installed around the ring to clear the electron cloud and to isolate areas of high electron-concentration. Electron detectors need to be installed at locations susceptible of high electron-concentration to monitor the electron production (Figure 18).
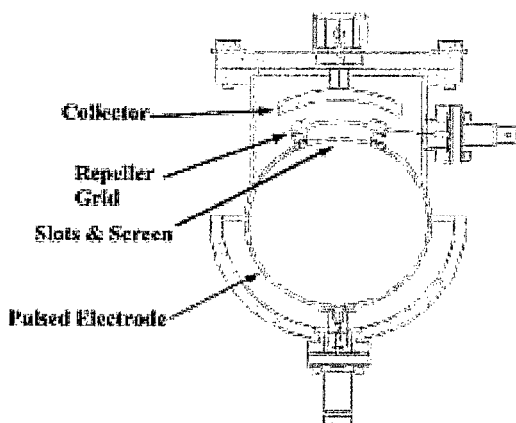

Figure 18: Electron sweeping detector developed at LANL's PSR (courtesy A. Browman).

Enhancement of Landau damping starts with the design of the machine. A large vacuum-pipe aperture is needed, especially at locations of high dispersion to allow further increase in momentum spread. A large RF voltage is required to provide the momentum acceptance. Longitudinal painting can be used to expand the injecting beam's momentum-spread. Devices like the inductive insert can be used to compensate for the space-charge effect, effectively increasing the RF focusing [57]. Landau-damping octupoles (KEK PF and BEPC) has been shown to raise the stability threshold. Lattice sextupole families (BEPC, SPS, KEKB, and SNS) can be used for chromatic adjustments, to either improve momentum acceptance [58] or enhance damping. Finally, a fast, wide-band feedback system can be implemented to damp instabilities.

6.1 Surface Treatment

Surface coating of TiN was shown to effectively suppress the electron flux by a factor of more than 100 at a coated section of the PSR (Figure 5). The thickness of the coating, typically about 100 nm, is chosen to withstand the bombardment of the electrons during the lifetime of the machine operation. For critical devices, e.g., the extraction kicker's ferrite residing inside the vacuum pipe (SNS), the pattern and thickness of the coating are chosen to avoid eddy-current heating and to prevent changes in material property. Planned, long-term bombardment with cold electrons further reduces the secondary-emission yield. Evidence of this "surface scrubbing" was seen at SPS, KEKB, and PSR. The memory of the scrubbing may be preserved by a Nitride glow discharge [59].

6.2 Clearing Electrodes

Clearing electrodes were shown to suppress the electron multipacting at CERN's ISR. At the SNS accumulator ring, the BPMs around the ring are designed to be also used as clearing electrodes capable of possessing a voltage of up to ±1 kV (Figure 19). Such a voltage overcomes the energy gain due to the proton bunch (Eq. 13). A dedicated clearing-electrode is implemented inside the stripping-foil assembly at the injection region.
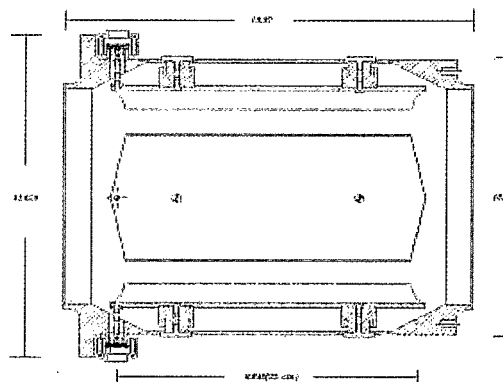

Figure 19: Schematics of the floating-ground BPM designed for the SNS accumulator ring (courtesy P. Cameron). A voltage of about ±1 kV can be applied for the clearing of the electron cloud.

6.3 Solenoids

Weak solenoids were shown to effectively improve machine operation under the electron-cloud at KEKB and PEP-II. In a short test-section at the PSR, a weak solenoid is found to suppress the electron flux (f_e) by a factor of about 50. For future high-intensity synchrotrons, such solenoids can also be used at straight sections, like the collimation section, to suppress electron generation. The

solenoid field B_ϕ needs to be strong enough so that the radius r_ϕ of electron motion is small compared with the vacuum-pipe radius [7]

$$r_\phi = \frac{m_e v_e}{e B_\phi} \ll b \qquad (21)$$

Effects on the proton beam can be minimized by alternating the polarities of the solenoids according to the betatron phase ϕ_x and ϕ_y [60]. Skew quadrupoles can further be used to correct the coupling according to the relation

$$-\sum_{sq} \frac{\sqrt{\beta_x \beta_y}}{f_{sq}} \begin{bmatrix} \cos \Delta\phi \\ \sin \Delta\phi \end{bmatrix} = \sum_{sol} g_\phi \theta_\phi \begin{bmatrix} \cos(\Delta\phi + \omega_\phi) \\ \sin(\Delta\phi + \omega_\phi) \end{bmatrix} \qquad (22)$$

where $\Delta\phi \equiv \phi_x - \phi_y$,

$$g_\phi = \sqrt{\gamma_x \beta_y + \gamma_y \beta_x + 2(1 - \alpha_x \alpha_y)} \qquad (23)$$

$$\tan(\omega_\phi) = \frac{\beta_x + \beta_y}{\alpha_x \beta_y - \alpha_y \beta_x}, \quad \theta_\phi = \frac{B_\phi L_\phi}{B_0 \rho} \qquad (24)$$

f_{sq} is the focal length of the skew quadrupole, L_ϕ is the length of the solenoid, $B_0 \rho$ is the regidity of the proton beam, and $\alpha_{x,y}$, $\beta_{x,y}$, and $\gamma_{x,y}$ are Courant-Snyder lattice functions.

7 SUMMARY

Electron-cloud effects are of primary concern to the operation of high-intensity proton synchrotrons and accumulator rings. During the last decade, significant progresses have been made in the studies of both electron generation and electron-proton dynamics. However, quantitative understanding is still lacking, especially in the prediction of instability threshold and growth rates.

Some open, challenging tasks include: (1) establishing a coupling-impedance model for the electron cloud when trailing-edge multipacting is dominant; (2) identifying the leading instability drive in the presence of a strong space-charge force among the protons; (3) predicting the detailed distribution of electron neutralization inside the proton bunch; (4) a self-consistent treatment of electron production and electron-proton interaction; (5) fully reproducing the experimental observation in high-intensity rings like the PSR; and (6) predicting the electron-cloud effects for next-generation high-intensity machines like the SNS accumulator ring and the JAERI/KEK Joint Project synchrotrons [61].

8 ACKNOWLEDGEMENTS

9 REFERENCES

[1] R. Macek, Workshop on Two-Stream Instabilities, Sante Fe (1999).

[2] E. Mètral, R. Cappi, M. Giovannozzi, G. Mètral, F. Zimmermann, Proc. 2001 Particle Accelerator Conference, Chicago (2001), p. 682.

[3] G. Arduini, V. Baglin, O. Bruening, R. Cappi, F. Caspers, P. Collier, I.R. Collins, K. Cornelis, R. Garoby, O. Groebner, B. Henrist, N. Hilleret, W. Hoefle, J.M. Jimenez, J-M. Laurent, T. Linnecar, E. Mercier, M. Pivi, F. Ruggiero, G. Rumolo, C. Scheuerlein, J."Tuckmantel, L. Vos, F. Zimmermann, *Electron-cloud effects in the CERN SPS and LHC*, Proc. 2000 European Particle Accelerator Conference, Vienna (2000), p. 1611.

[4] J. Wei, D. T. Abell, J. Beebe-Wang, M. Blaskiewicz, P. R. Cameron, N. Catalan-Lasheras, G. Danby, A. V. Fedotov, C. Gardner, J. Jackson, Y. Y. Lee, H. Ludewig, N. Malitsky, W. Meng, Y. Papaphilippou, D. Raparia, N. Tsoupas, W. T. Weng, R. L. Witkover, S. Y. Zhang, *Low-loss design for the high-intensity accumulator ring of the Spallation Neutron Source*, Phys. Rev. ST-AB, **3** (1999), p. 080101.

[5] *The LHC Conceptual Design Report*, CERN/AC/95-05(LHC), CERN (1995).

[6] *The Relativistic Heavy Ion Collider Design Manual*, Brookhaven National Laboratory (1994).

[7] S. Y. Zhang, Private communications.

[8] W. Fischer, talk presented at the Workshop ECLOUD'02, CERN (2002).

[9] M. Blaskiewicz, AIP Conference Proceedings **496**, edited by T. Roser and S.Y. Zhang (AIP, N.Y. 1999), p. 321.

[10] R. J. Macek, A. Browman, D. Fitzgerald, R. McCrady, F. Merrill, M. Plum, T. Spickermann, T.S. Wang, J. Griffin, K.Y. Ng, D. Wildman, K. Harkay, R. Kustom, R. Rosenberg, *Electron proton two-stream instability at the PSR*, Proc. 2001 Particle Accelerator Conference, Chicago (2001), p. 688.

[11] R.Rosenberg and K.Harkay, Nucl. Instrum. Methods, **A 453** (2000), p. 507.

[12] T. Tabata, R. Ito, and S. Okabe, Nucl. Instrum. Methods, **94** 1971, p. 509.

[13] M. Plum, *Electric fields, electron production, and electron motion at the stripper foil in the Los Alamos Proton Storage Ring*, Proc. 1995 Particle Accelerator Conference, Dallas (1995), p. 3403.

[14] J. Brodowski, private communications (2002).

[15] P. Thieberger, A. L. Hanson, D. B. Steski, V. Zajic, S. Y. Zhang, H. Ludewig, Phys. Rev., **A61** (1999), p. 042901.

[16] J. Shou, *Transport theory for kinetic emission of secondary electron from solids*, Phys. Rev., **B27** (1980), p. 2141.

[17] H. Seiler, J. Appl. Phys., **54** (1983), p. R1.

[18] J.E. Borovsky, D.J. McComas, and B.L. Barraclough, *The secondary-electron yield measured for 5-24 MeV protons on aluminum-oxide and gold target*, Nucl. Instrum. Methods, **B30** 1988, p. 191.

[19] H. Ludewig, N. Simos, J. Walker, P. Thieberger, A. Aronson, J. Wei, *Collimator system for the SNS accumulator ring*, Proc. 1999 Particle Accelerator Conference, New York (1999), p. 548.

[20] O. Gröbner, HEACC'77, Protvino (1977), p. 277.

[21] F. Zimmermann, *A simulation study of electron-cloud instability and beam-induced multipacting in the LHC*, LHC Project-Report 95, and SLAC-PUB-7425 (1997).

[22] M. A. Furman and G. R. Lambertson, *The electron cloud effect in the arcs of the PEP-II positron ring*, KEK Proceedings 97-17, p. 170, (Proc. MBI97 workshop, KEK, Y.H. Chin, ed.) (1997).

[23] O. Gröbner, *Beam induced multipacting*, Proc. 1997 Particle Accelerator Conference, Vancouver (1997), p. 3589.

[24] F. Ruggiero, G. Rumolo, F. Zimmermann, *Simulation of the electron-cloud build up and its consequences on heat load, beam stability and diagnostics*, Phys. Rev. ST-AB **2** (2001), p. 012801, Erratum-ibid. (2001), p. 029901.

[25] V. Danilov, et al., *Multipacting on the trailing edge of proton beam bunches in the PSR and SNS*, AIP Conference Proceeding 496, edited by T. Roser and S.Y. Zhang (AIP, N.Y. 1999), p. 315.

[26] F. Zimmermann, *The electron cloud instability: summary of measurements and understanding*, Proc. 2001 Particle Accelerator Conference, Chicago (2001), p. 666.

[27] M. Pivi, M. Furman, Proc. Workshop on Electron-Cloud Simulations for Proton and Positron Beams, CERN (2002, to be published).

[28] R. Kirby et al, SLAC-PUB-8212, Stanford University (2000).

[29] V. Danilov, A. Aleksandrov, J. Wei, M. Blaskiewicz, *Calculations of the electron accumulation in the SNS storage ring*, Proc. 2001 Particle Accelerator Conference, Chicago (2001), p. 1749.

[30] K. Ohmi, *Beam and photoelectron interactions in positron storage rings*, Phys. Rev. Lett. 75 (1995), p. 1526.

[31] M. A. Furman et al, KEK Proc. 97-17 (1997), p. 170.

[32] M. Blaskiewicz, *Implications of the PSR instability for the SNS*, Proc. 2000 European Particle Accelerator Conference, Vienna (2000), p. 1110.

[33] K. Ohmi, L. F. Wang, H. Fukuma, K. Ohmi, Y. Suetsugu, *3D simulation of photoelectron cloud*, Proc. 2001 Particle Accelerator Conference, Chicago (2001), p. 701.

[34] N. Malitsky, J. Smith, J. Wei, R. Talman, Proc. 1999 Particle Accelerator Conference, New York, edited by A. Luccio and W. MacKay (1999), p. 2713.

[35] L. J. Laslett, *Workshop on Injection and Extraction*, BNL Report 7534 (1963), p. 324.

[36] H. Hereward, Workshop on Injection and Extraction, CERN Report 71-15 (1971).

[37] E. Keil and B. Zotter, Workshop on Injection and Extraction, CERN Report CERN-ISR-TH-71-58 (1971).

[38] D. Neuffer, *Observations of a fast transverse instability in the PSR*, Nucl. Instrum. Methods, A321 (1992), p. 1.

[39] L.D. Landau, J. Physics USSR, **10** (1946), p. 25.

[40] T.S. Wang, P.J. Channell, R. Macek, R.C. Davidson, Proc. 2001 Particle Accelerator Conference, Chicago (2001), p. 704.

[41] R.C. Davidson, H. Qin, P.J. Channell, Phys. Rev. ST-AB, **2** (2001), p. 074401.

[42] M. Izawa, Y. Sato, and T. Toyomasu, *The vertical instability in a positron bunched beam*, Phys. Rev. Lett. 74 (1995), p. 5044.

[43] Z.Y. Guo et al., *Study of the beam-photoelectron instability in BEPC*, KEK-PREPRINT-98-23, Proc. 1st Asian Particle Accelerator Conference, Tsukuba (1998).

[44] G. Arduini, K. Cornelis, W. Hoefle, G. Rumolo, F. Zimmermann, *Transverse behavior of the LHC proton beam in the SPS: an update*, Proc. 2001 Particle Accelerator Conference, Chicago (2001), p. 1883.

[45] K. Ohmi et al, Proc. 2001 High Energy Accelerator Conference, Tsukuba (2001).

[46] T. Raubenheimer et al, Phys. Rev. **E52** (1995), p. 5487.

[47] F. Zimmermann, *Electron-cloud studies for the low energy ring of KEKB*, CERN-SL-NOTE-2000-004 AP (2000).

[48] K. Ohmi and F. Zimmermann, *Head-tail instability caused by electron cloud in positron storage rings*, Phys. Rev. Letters, **85**, p. 3821.

[49] K. Ohmi, F. Zimmermann, E. Perevedentsev, *Wake field and fast head-tail instability caused by an electron cloud*, Phys. Rev., E **65** (2002), p. 016502.

[50] G. Rumolo, F. Zimmermann, *Simulation of single bunch instabilities driven by electron cloud in the SPS*, Proc. 2001 Particle Accelerator Conference, Chicago (2001), p. 1889.

[51] K. Ohmi, *Particle-in-cell simulation of beam-electron cloud interactions*, Proc. 2001 Particle Accelerator Conference, Chicago (2001), p. 1895.

[52] R. Nawrocky et al, Proc. 1993 Particle Accelerator Conferences, Washington, D.C. (1993), p. 2145.

[53] R. L. Witkover, P. R. Cameron, T. J. Shea, R. C. Connolly and M. Kesselman, Proc. 1999 Particle Accelerator Conference, New York, edited by A. Luccio and W. MacKay (1999), p. 2150.

[54] N. Catalan-Lasheras, Y. Y. Lee, H. Ludewig, N. Simos, J. Wei, *Optimization of the collimation system for the Spallation Neutron Source accumulator ring*, Phys. Rev. ST-AB, **4** (2001), p. 010101.

[55] Y. Funakoshi, Y. Funakoshi, K. Akai, N. Akasaka, K. Bane, A. Enomoto, J. Flanagan, H. Fukuma, K. Furukawa, J. Haba, S. Hiramatsu, K. Hosoyama, T. Ieiri, N. Iida, T. Kamitani, S. Kato, M. Kikuchi, E. Kikutani, H. Koiso, S.I. Kurokawa, M. Masuzawa, T. Matsumoto, S. Michizono, T. Mimashi, T. T. Nakamura, Y. Ogawa, K. Ohmi, Y. Ohnishi, S. Ohsawa, N. Ohuchi, K. Oide, E. A. Perevedentsev, K. Satoh, M. Suetake, Y. Suetsugu, T. Suwada, F. Takasaki, M. Tawada, M. Tejima, M. Tobiyama, N. Yamamoto, M. Yoshida, S. Yoshimoto, M. Yoshioka, C. H. Yu, F. Zimmermann, *KEKB performance*, Proc. 2000 European Particle Accelerator Conference, Vienna (2000), p. 28.

[56] S.-I. Kurokawa, *B-factory commissioning and first result*, Proc. 2001 Particle Accelerator Conference, Chicago (2001), p. 6.

[57] K. Y. Ng, D. Wildman, M. Popovic, A. Browman, D. Fitzgerald, R. Macek, M. Plum, T. Spickermann, *Recent experience with inductive insert at PSR*, Proc. 2001 Particle Accelerator Conference, Chicago (2001), p. 2890.

[58] N. Tsoupas, C. Gardner, Y. Y. Lee, Y. Papaphilippou, J. Wei, *Chromatic correction and optical compensation in the SNS accumulator ring using sextupoles*, Proc. 2000 European Particle Accelerator Conference, Vienna (2000), p. 1581.

[59] J. M. Jimenez, Chamonix XI, CERN-SL-2001-003-DI (2001).

[60] S. Peggs, *Coupling and decoupling in storage rings*, IEEE Transactions, **NS-30** (1983), p. 2460.

[61] *JHF Accelerator Design Report*, KEK Rport 97-16, JHF-97-10 (1998).